Jet stream variability in a polar warming scenario - a laboratory perspective

Costanza Rodda[1,2], Uwe Harlander[1], and Miklos Vincze[3]

[1]Brandenburg University of Technology Cottbus–Senftenberg, Department of Aerodynamics and Fluid Mechanics, Cottbus, D-03046, Germany
[2]Department of Civil and Environmental Engineering, Imperial College London, London SW7 2AZ, England, United Kingdom
[3]von Kaŕmán Laboratory of Environmental Flows; Eötvös Loránd University, Budapest H-1117, Hungary/ MTA-ELTE Theoretical Physics Research Group; Eötvös Loránd University, Budapest H-1117, Hungary

Correspondence: Costanza Rodda (c.rodda@imperial.ac.uk)

Abstract.

We report on a set of laboratory experiments to investigate the effect of polar warming on the mid-latitude jet stream. Our results show that a progressive decrease of the meridional temperature difference slows down the eastward propagation of the jet stream and complexifies its structure. Temperature variability decreases in relation to the laboratory 'Arctic warming' only at locations representing the Earth's polar and mid-latitudes, which are influenced by the jet stream, whilst such trend reverses in the subtropical region south of the simulated jet. The reduced variability results in narrower temperature distributions and hence milder extreme events. However, our experiments also show that the frequency of such events increases at polar and mid-latitudes with decreased meridional temperature difference, whilst it decreases towards the subtropics. Despite missing land-sea contrast in the laboratory model, we find qualitatively similar trends of temperature variability and extreme events in the experimental data and the National Centers for Environmental Prediction (NCEP) reanalysis data.

1 Introduction

Since 1980, the polar regions have been warming approximately twice as fast as the mid-latitudes in the Northern Hemisphere, a phenomenon known as Arctic warming amplification. Model simulations (the 40-member CCSM3 ensemble) imply that this trend will continue in the future due to a robust global warming signal (Wallace et al., 2014). The signal-to-noise ratio is relatively small at higher latitudes and more significant in the tropics. Despite its well-established presence, there is still a debate about the leading causes of Arctic warming amplification. Different models suggest that sea-ice loss, lapse-rate feedback, or increasing downwelling radiation at the surface could be the main contributor (Stuecker et al., 2018).

Regardless of the causes, it is unclear whether this faster Arctic warming impacts the large-scale circulation and, if so, the effects of such changes on extreme events. Francis and Vavrus (2015) found that the Arctic amplification enlarges the North-South meandering of the mid-latitude jet-stream and causes a slow down in the eastward progression of Rossby waves. These waves are closely connected to the spatio-temporal distribution of extreme weather events. Cold outbreaks, for instance,

occur when the crests of Rossby waves penetrate lower latitudes, whilst heat waves may develop at their troughs. A slower progression of Rossby waves impacts extreme weather events- heatwaves, heavy downpours, and hurricanes- by increasing their duration.

25   Other studies have reported a reduction in the mid-latitude temperature variability, suggesting that the previously observed increase in meandering has reversed its course and questioning whether it is caused by internal variability or arctic amplification (Blackport and Screen, 2020; Dai and Deng, 2021). A lowered variability of the future mid-latitude weather would lead to less extreme temperatures.

The two major wave features that have been connected to extreme events and Arctic warming are quasi-resonant amplifica-
30   tion of Rossby waves trapped in a waveguide and blocking (Petoukhov et al., 2013), a persistent pressure anomaly that prevents the usual zonal propagation of atmospheric perturbations (Benzi et al., 1986). The latter is connected to Arctic warming, assuming that a reduced temperature gradient leads to slowing down the background westerlies and the eastward progressing Rossby waves. Hence, blocking and extreme events become more likely. For example, Screen and Simmonds (2014) report a higher frequency of extreme events in coincidence with high-amplitude planetary waves that seem to favour the occurrence of ex-
35   treme weather. Other studies, however, indicate a decrease in blocks due to the decreasing the mid-latitude to pole temperature difference (Hassanzadeh et al., 2014).

These contrasting results point toward the need for more studies to help resolve the matter of Arctic amplification consequences on the mid-latitude weather. However, the complex dynamics of the atmosphere and the multiple influences and feedbacks pose severe difficulties in finding a final answer (Overland et al., 2016). The analysis of historical changes and fully
40   coupled model simulations is particularly challenging because many of these phenomena are correlated and, therefore, cause and effect are difficult to distinguish through regression or correlation analysis (Dai and Song, 2020).

Laboratory experiments enable us to isolate the two key elements of mid-latitude variability from any other feedback process. Such isolation is fundamental in understanding the dynamical cause-effect connection. Furthermore, laboratory experiments are repeatable and can simulate very long time series, providing a statistically significant data set. Hence, we propose an
45   experimental study to complement the widely used observational data. The differentially heated rotating annulus is a simple experiment that captures the essential dynamical processes driving the circulation of the terrestrial atmosphere at mid-latitudes, particularly the large-scale waves and the meandering of the jet stream. Such a laboratory model has been extensively used to understand the mechanism generating large-scale atmospheric waves (baroclinic waves): the so-called sloping convection (Hide, 1958; Read et al., 2014). The combined effect of the radial temperature difference produced by two thermal baths,
50   analogous to the pole-to-equator temperature gradient, and the rotation of the tank, analogous to the planetary rotation, reproduce the fundamental physical forcing of the atmospheric large-scale overturning circulation. Under certain combinations of temperature difference and rotation, the baroclinic instability can develop in the middle gap giving rise to baroclinic waves and driving the formation of the jet stream. In its most used configuration, the experiment captures the essential aspects of the dynamics and does not include other processes that bring secondary effects into the dynamics, among which is the β-effect.

55   Over many years, these laboratory experiments have played a prominent role in geophysical fluid dynamics and climate studies. Several examples are given in the review article by Vincze and Jánosi (2016), such as investigating asymmetries of

atmospheric temperature fluctuations and experiments on interdecadal climate variability. The emerging scenario reveals that local variability, e.g. in Western Europe or North America, has increased in the past 40 years. Vincze et al. (2017) investigated the nature of connections between external forcing and climate variability conceptually using a laboratory experiment subject to continuously decreasing 'pole-to-equator' temperature contrast ΔT. Finally, Rodda and Harlander (2020) recently demonstrated the potential for using laboratory data to study multiple-scale interactions and explain even mesoscale atmospheric processes. Their study reveals that frequency spectra from the differentially heated annulus experiment are comparable to the power spectra from atmospheric field observations.

The paper is structured as follows. In section 2, we briefly describe the experiment, and in section 3, we give insight into typical flow regimes of the annulus experiment. We further study the impact of polar warming on the wave train structure and zonal phase speed. In sections 4 and 5, we focus on statistical properties that depend on the temperature. Section 4 is the core of this paper, where we investigate the temperature distributions and the impact of polar warming on extreme event frequency from experimental data. We then inspect and compare some of these features in NCEP reanalysis data in section 5. Finally, in section 6, we offer our concluding remarks.

2 Experimental apparatus and measurements

The experiments presented in this paper have been run with a differentially heated rotating annulus at the BTU Cottbus-Senftenberg laboratories (see von Larcher and Egbers (2005) for more details about the experimental apparatus). The experimental setup, sketched in Fig. 1, consists of a cylindrical tank divided into three concentric rings filled with de-ionised water. The inner cylinder has a radius of $a = 4.5$ cm and is made of anodised aluminium. The water filling the inner cylinder is cooled by an external thermostat connected to the experiment. The tank is made of borosilicate glass, and the outer ring is separated from the middle cavity by a wall placed at radial distance $b = 12$ cm. Heating wires, supplied with constant power by a control unit, warm the water in the outer ring. The mid-gap (of width $b - a = 7.5$ cm) is filled up to the height $D = 5$ cm, and the fluid is subjected to a radial temperature difference ΔT imposed at the boundaries by the two thermally conducting walls. The tank is mounted on a turntable, which rotates counterclockwise around its vertical axis of symmetry at a constant rate Ω. The combined effect of the radial temperature difference produced by the two thermal baths and the rotation of the tank results in the set-in of the baroclinic instability in the middle gap giving rise to baroclinic waves. These waves developing in the annulus are analogous to the large-scale atmospheric waves, which shape the meandering of the mid-latitude jet stream.

Our experimental data set consists of nine separate runs that differ in the temperature set at the boundaries. The temperatures are increased for each successive experiment in a way that reproduces a warming scenario similar to the Arctic amplification in the experiment; namely, the cold bath temperature is increased on average 1.75 times more than the temperature in the hot bath. In the rest of the paper, we use the more general term 'polar warming' for this scenario. Sensors are placed in the outer warm and inner cold ring to measure the temperature in the two thermal baths, T_{cold} and T_{warm}, and calculate the radial temperature difference ΔT. Figure 2 and table 1 show the mean temperature measured by these sensors as a function of the temperature set
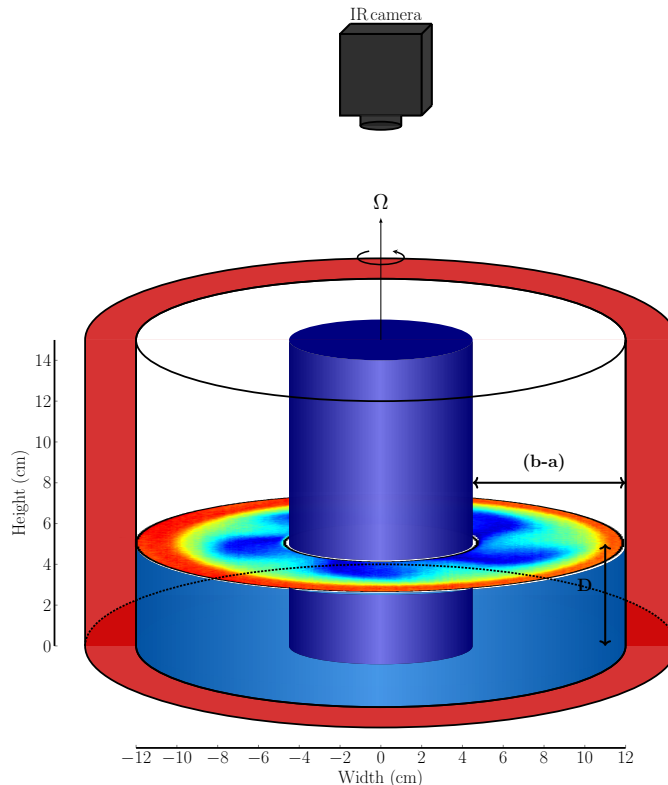
Figure 1. Schematic drawing of the experimental apparatus. The water in the inner cylinder (in blue) is cooled using a thermostat. Heating wires heat the water in the outer ring (in red). The water in the inner gap $(b-a)$ is subjected to a radial differential temperature inferred by the insulating walls. The tank rotates counterclockwise at a constant rotation rate Ω. The surface temperature of the fluid in the gap is measured by an infrared camera aligned with the axis of rotation.

in the cooling basin of the thermostat for each experimental run. It can be seen in Fig. 2 that the mean temperature increases throughout the runs. More details about the technical setting of the two thermal baths are given in Appendix A.

After the experiment reaches thermal equilibrium, we start the rotation rate Ω set to 8 rpm counterclockwise. The centrifugal Froude number, defined as $Fr = \Omega^2(b-a)/g$, where $(b-a)$ is the gap width, is in the order of 5×10^{-3} and hence much smaller than 1. The system is let run for the spin-up time (approximately two hours), after which it reaches a stable state. Then, the data are collected for seven hours, corresponding to ca. 3000 revolutions of the tank. Given that each revolution corresponds to one terrestrial day, our experiment simulates nine cases with different pole-to-equator temperature differences lasting each for little more than eight years in the lab-Earth analogy.

The surface temperature is measured with an Infrared Camera, IR camera in short (Jenoptik camera module IR-TCM 640, with thermal sensitivity of 0.01 K and image resolution 640×480 pixels). The IR camera is fixed in the laboratory reference system and mounted at the top of the experiment (see Fig. 1). The IR camera outputs are the time series of the entire annulus
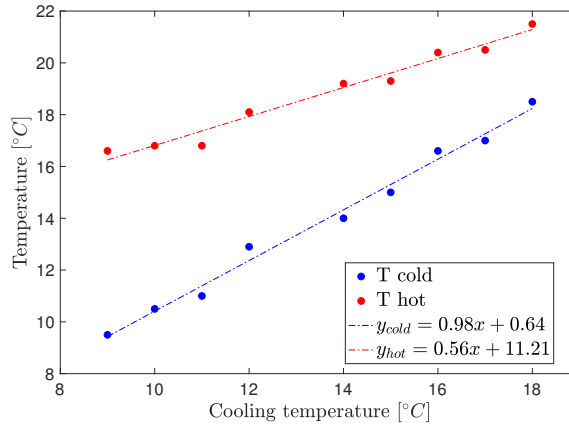
Figure 2. Temperature in the cold inner cylinder (blue) and hot outer ring (red) as a function of the cold thermostat target value. In the experiments discussed here (see Table 1), the temperature of the cooled water was increased 1.75 times more than the temperature of the heated water. The series of experiments form an Arctic amplification scenario with an increase in mean temperature but a decrease of the radial temperature gradient.

2D surface field measured once at each tank rotation, corresponding to a sampling interval $dt = 7.5$ s. The advantage of having the 2D field is that some characteristics, such as dominant wave patterns, zonal phase speed (i.e. the speed at which the pattern drifts as a whole anticlockwise around the apparatus in the rotating frame), and changes in the structure, can be detected. The spatial and temporal resolution are $400 \times 400 \times 3000$ (pixels and times, x, y, t).

3 Flow regimes

This section discusses the dependency of the flow regimes on the radial temperature difference ΔT. Understanding how changes in ΔT impact the spatio-temporal flow features is a necessary first step for examining the effects on the temperature distribution.

Two nondimensional similarity parameters control the flow behaviour in a differentially heated rotating annulus (Hide and Mason, 1975): the Taylor number

$$Ta = \frac{f^2(b-a)^5}{\nu^2 D},\tag{1}$$

and the thermal Rossby number

$$Ro_T = \frac{gD\alpha\Delta T}{f^2(b-a)^2}.\tag{2}$$

Here, g is gravity, $f = 2\Omega$ is the Coriolis parameter, $\Omega = 8$ rpm the tank rotation, $\alpha = 0.207 \times 10^{-3}$ K^{-1} the volumetric thermal expansion coefficient, $\nu = 1.004 \times 10^{-6}$ m^{2}s^{-1} the kinematic viscosity of water, $D = 0.05$ m the fluid depth, and $b-a = 0.075$
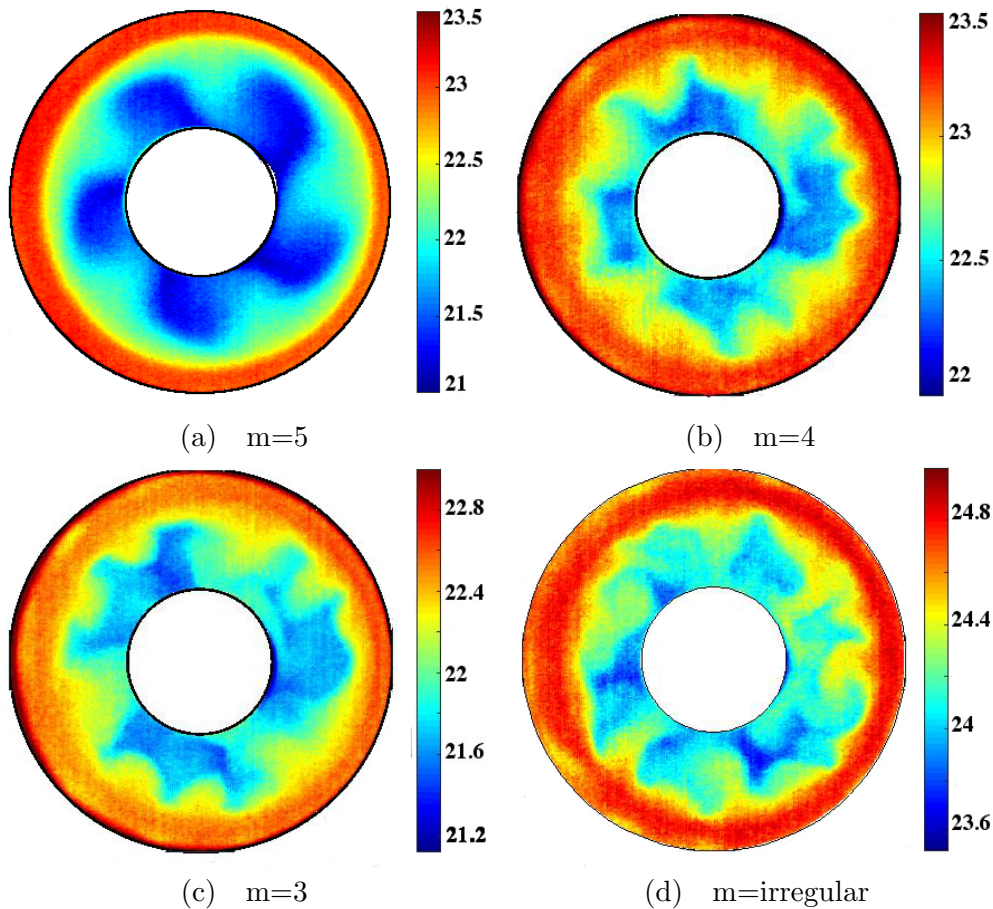
Figure 3. Flow regimes at $\Delta T = 7.1K$ (a), $\Delta T = 5.2K$ (b) and (c), and $\Delta T = 3K$ (d). The flow becomes more irregular for decreasing ΔT.

m the gap width. For relatively shallow fluid depths D, Rodda et al. (2020) found that the bottom Ekman layer has a significant impact on the dynamics of the flow and hinders the formation of baroclinic waves. For the experiments presented here, we chose a fluid depth such that the bottom drag is negligible.

A typical regime diagram can be drawn in the $Ta - Ro$ space with the identification of flow regimes (Hide and Mason, 1975). Ro_T and Ta higher than the lower critical value define an anvil-shaped region where regular baroclinic waves develop in the fluid. Increases in Ta and decreases in Ro_T lead the flow towards a more irregular regime until it fully transitions to geostrophic turbulence, in which complex nonlinear wave interactions arise and the flow is irregular and non-periodic in time and space. Since we kept the tank rotation constant, the Taylor number, $Ta = 1.32 \times 10^8$, is constant as well and $Ro_T \sim \Delta T$.

Table 1. Overview of the experimental runs. T_C is the temperature of the cooling thermostat. T_{cold} and T_{warm} are the measured temperatures in the inner and outer ring respectively. $\overline{T} = (T_{\mathrm{warm}} + T_{\mathrm{cold}})/2$ is the mean temperature. $\Delta T = T_{\mathrm{warm}} - T_{\mathrm{cold}}$ is the radial temperature difference. m is the azimuthal wavenumber of the baroclinic wave, and I indicates irregular waves. The rotation rate is $\Omega = 8$ rpm for all runs. Ro_T is the thermal Rossby number (2). The Taylor number (1) is $Ta = 1.32 \times 10^8$.

Name	T_C	T_{cold}	T_{warm}	$\overline{T}$	ΔT	m	Ro_T
C18	18	18.5	21.5	20	3	I	0.019
C17	17	17	20.5	18.7	3.1	I (8-1)	0.020
C16	16	16.6	20.4	18.5	3.8	I (7-1)	0.024
C15	15	15	19.3	17.1	4.5	6-1	0.029
C14	14	14	19.2	16.6	4.8	6-2	0.034
C12	12	12.9	18.1	15.5	5.2	6-3	0.034
C11	11	11	16.8	13.9	5.8	6-2	0.037
C10	10	10.5	16.8	13.6	6.3	5-3	0.040
C9	9	9.5	16.6	13	7.1	5-4	0.046

Table 1 lists the experimental runs and their parameters. T_C is the temperature of the cooling thermostat. T_{cold} and T_{warm}
125 are the mean temperatures measured by sensors placed in the inner cold cylinder and warm outer ring, respectively, once a constant temperature difference ΔT is reached. Due to T_C rising, the mean temperature in the gap $\overline{T}$ (resulting from a thermal equilibrium between the boundary walls) increases, even though the heating power supply to the outer ring is kept constant. T_{cold} and T_{warm} are plotted in Fig. 2 as a function of T_C. It can be noticed that T_{cold} (in blue) increases 1.75 times more than T_{warm} (in red in figure 2). This temperature change is well suited to experimentally mimic the polar warming effect observed
130 in the atmosphere.

3.1 Wavenumber transitions

It is enlightening to study the effects of lowering Ro_t on the flow regimes in the azimuthal wavenumber space. For our experiments $Ta = 1.32 \times 10^8$. Other experiments in similar setups have identified the threshold between regular baroclinic waves and geostrophic turbulence at $Ta \approx 10^8$ (Harlander et al., 2011b). Close to this transition, the flow becomes more
135 complex due to the nonlinear interactions between the dominant mode and sidebands, resulting in mixed mode states, and therefore the behaviour of the flow becomes less predictable (Früh and Read, 1997). Figure 3 displays surface temperature snapshots taken with the IR camera during different experimental runs and gives examples of flow regimes. Run C9 (Fig. 3 (a)) is in a regular baroclinic wave regime with a regularly shaped wave at wavenumber $m = 5$. With smaller ΔT the complex interactions among waves result in wider spectra spanning several wavenumbers, as can be seen in Fig. 4, which shows
140 the time evolution of the azimuthal wavenumber determined by calculating the spatial Fourier transform of the temperature data measured with a sampling rate of $\Delta t = 3.75$ s along a constant radius $r_0 = 0.063$ m. In experiment C15 (Fig. 4 (a)),

(a) $\Delta T = 4.5$ [°C]   (b) $\Delta T = 3$ [°C]
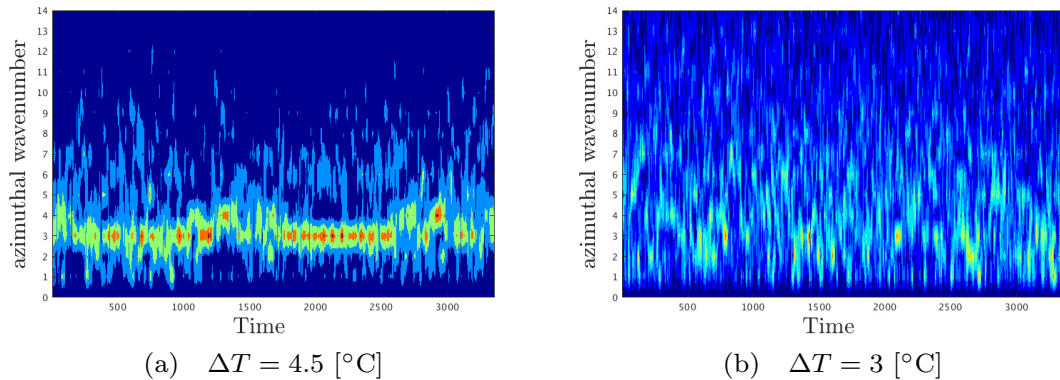
Figure 4. Azimuthal wavenumber evolution over time for experiments C15 (a) and C18 (b). The colormap represents the Fourier transform of temperature data sampled at a constant radius $r_0 = 0.063$ m. Larger ΔT are associated to flows with a dominant wavenumber where sporadic transitions occur over time (a). When ΔT is decreased the flow is irregular as a result of a superposition of wavenumbers (b).

the dominant wavenumber switches between $m = 3$ and $m = 4$ with sporadic transitions to higher and lower wavenumbers ranging between $m = 6$ and $m = 1$. This behaviour resembles that often referred to as structural vacillation in the baroclinic wave literature (Hide and Mason, 1975). For decreasing Ro_T, it becomes more and more difficult to establish the dominant wavenumber associated with the flow, as several transitions among other m occur over time. In table 1, we have indicated the range of observed wavenumbers in the column marked by m. One can easily see that the range of wavenumbers broadens with decreasing ΔT. As it can be seen for experiment C18 (Fig. 4 (b)), the flow is in a noticeably more irregular state, with a broad spectrum of excited wavenumbers. In the latter regime, it is challenging to identify a dominant azimuthal wavenumber m. We refer to this state as irregular (indicated by I in table 1), where the flow has developed into geostrophic turbulence.

3.2 Zonal phase speed

The zonal phase speed of the waves can be estimated by combining the thermal wind balance $U_T = Ro_T f L/4$ with (2)

$$U_T = \frac{g\alpha D \Delta T}{f(b-a)}. \tag{3}$$

The linear theory by Eady (1949) predicts that the zonal phase speed of an unstable baroclinic wave in a zonal shear flow $U = U_0 z$ (U_0 constant) of depth D is $c = DU_0/2$. It follows that baroclinic Eady waves are non-dispersive, and each wave mode drifts with the same speed. Previous experimental studies (Fein (1973); Vincze et al. (2015)) have observed that the measured zonal phase speed as a function of $\alpha \Delta T/f$ is better fitted by a more general power-law equation

$$c = B(\alpha \Delta T/f)^\zeta, \tag{4}$$
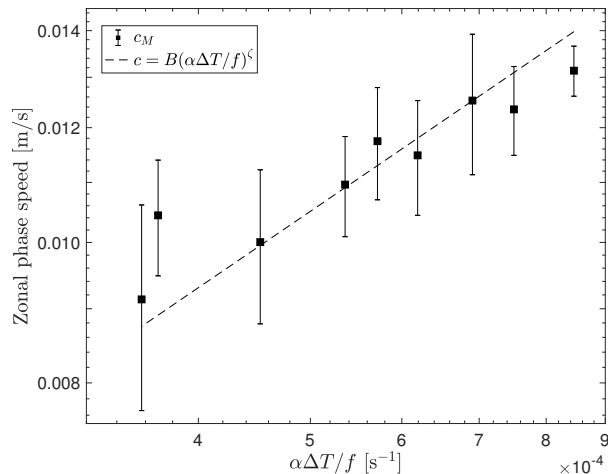
Figure 5. Log-log plot of the zonal phase speed c_M of the baroclinic wavefront for decreasing ΔT calculated from ϕ-t diagrams at a fixed radius $R_d = 0.087$ m. The dashed line c is calculated from (4) with $\zeta = 0.55$.

with $B = gD/(b-a)$ a constant depending on the experimental configuration and the exponent ζ an empirical parameter. Note that for $\zeta = 1$, we obtain $c = U_T$ given by (3). The Eady model can be used to make some quantitative predictions for the experimentally observed baroclinic waves, keeping in mind that the model is highly idealised and therefore some differences can be expected. The experiment has a free surface and bottom Ekman layer, therefore the zonal velocity, U, is not simply a linear function of z. Moreover, due to the lateral walls, the mean flow shows also a shear in the radial direction. Finally, rotation and the curvature of the side walls lead to slight free surface deformation. These effects, taken together, introduce a weak dispersion to the baroclinic waves. Low-frequency vacillations might result from this dispersion even without nonlinear interactions, as discussed in detail by Harlander et al. (2011a). Therefore, the zonal phase speed of the baroclinic wavefront, in our experiment taken as the contourline of the maximum velocity gradient along the radial direction, is challenging to predict, especially in regimes in which the dominant wavenumber is changing over time (see figure 4). In general, the zonal phase speed c_M can be defined as:

$$c_M = \frac{1}{m}\frac{d\Phi}{dt} = \frac{1}{m}\omega = \frac{\lambda}{T_p}, \tag{5}$$

where $\Phi = \boldsymbol{k}\boldsymbol{x} - \omega t$ is the phase of a wave, $\omega = d\phi/dt, \lambda = 2\pi/m, T_p = 2\pi/\omega$ are wave frequency, wavelength, and period, respectively. If we use the linear theory proposed by Eady, the waves can be assumed to be travelling with the same speed of the background flow and therefore $c_M \approx U_T$. To calculate c_M from the temperature data, we have extracted the temperature along a fixed radius R_d and plotted them as a function of time. In this way, we obtain a Hovmöller diagram with the azimuthal coordinate ϕ on the $y-$axis and time on the $x-$axis from which we can calculate the zonal phase speed graphically. The wavefronts appear in this plot as tilted lines of maximum temperature, and their slope is the zonal phase speed at which the baroclinic wave travels. We obtained the drift speeds by measuring the slope of ten wavefronts and then calculating the mean

value and the associated standard deviation. This procedure is repeated for each experimental run associated with a different ΔT.

The mean zonal phase speed c_M with the associated error is plotted in figure 5 as a function of $\alpha \Delta T / f$. It is evident that decreasing ΔT slows down the zonal phase speed of the baroclinic waves. The dashed line in figure 5 depicts the general power-law equation (4), where we calculated the coefficient $\zeta = 0.55$ by fitting the data. Figure 5 also shows that qualitatively the predictions from linear wave theory carry over to large-amplitude nonlinear waves. The zonal phase speed c predicted by (4) is close to the experimentally measured c_M, particularly for the regular flow regimes with a zonal wavenumber $m = 4$ wave (the intermediate values of ΔT in runs C11-C15, see table 1).

Compared with Eady waves, dispersive Rossby waves are slower than the mean background flow for beta > 0. Note that a sloping topography can produce a beta < 0, leading to faster propagation than the background flow. This holds in particular for long waves. Thus, from the zonal phase speed results, we can conclude that the effect of decreasing the radial temperature difference is to slow down the baroclinic wavefront. Hence, the propagation speed of extreme events embedded into the wave trains, e.g. in the form of exceptional large meanders, will be slowed down, and the events in real atmospheric flows might unfold their local destructive potential over a more extended period.

4 Temperature distributions and variability

This section investigates how polar amplification affects temperature distributions, mainly focusing on the variability.

Figure 7 compares the probability density distributions of the temperature anomalies for all nine experimental runs. Temperature anomalies are calculated by subtracting the mean temperature from the measurements at each location 'p', 'm', and 'e'. Distributions at all three locations present a visible deviation from Gaussianity, which is more pronounced for larger ΔT. Noticeably, the polar and middle regions are characterised by broader temperature distributions, whilst the distribution in the outer region is much narrower. This difference tends to be less marked for smaller ΔT. For the polar and middle regions (left and middle plots), temperature variability consistently decreases for decreasing ΔT (red lines), with narrower and more symmetric distributions. In the subtropical regions, the tendency is the exact opposite: the distributions broaden for decreasing ΔT. The run "C9", at the highest ΔT, stands out for its double-peaked distributions at all latitudes, which are also much broader than all other runs.

The changes in temperature anomalies variability are quantified in Fig. 8, where standard deviation (left), skewness (middle), and excess of kurtosis (right) are plotted for the distributions at the three latitudes shown in Fig. 7.

The standard deviation decreases with decreasing ΔT in the polar and mid-latitude regions (blue and black lines), whilst it increases in the proximity of the subtropics (red line). To establish the statistical significance of the trends, we calculated the p-value with the t-test of the fit linear regression model `fitlm`, considering the 95% significance level. Hence, we consider trends with $p < .05$ as statistically significant, meaning that there is a probability higher than 95% that the corresponding coefficient is different from zero.
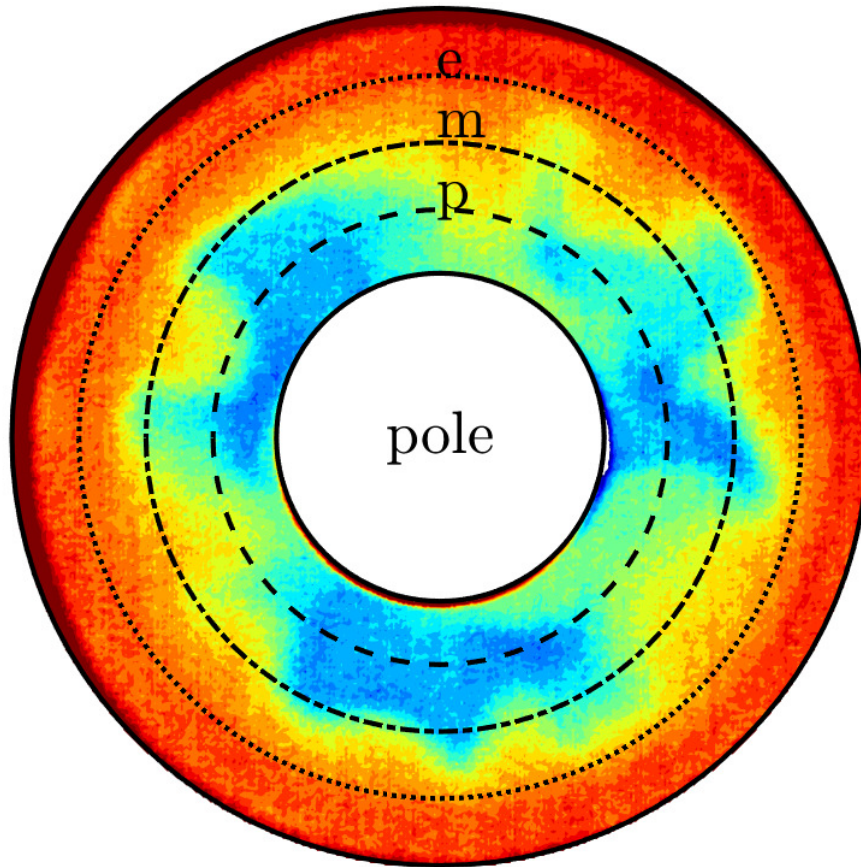
Figure 6. Three regions of the domain and location of the baroclinic wave: polar region (between the inner ring and the circle marked with 'p'), mid-latitudes (between 'p' and 'm'), and subtropical regions (between 'e' and the outer ring). The colours show the temperature measured for the experiment at $\Delta T = 4.5$.

The negative trends of the standard deviation are statistically significant ($p = .01$ for the polar region and $p = .003$ for the middle region), but the positive trend in the subtropical region is nonsignificant ($p = .11$). Note that the data point corresponding to the highest ΔT has been ignored to calculate the trends in Fig. 8 since it lies far off all the other data points. These points correspond to the double-peaked distributions in Fig. 7.

The excess kurtosis in Fig. 8 (right) shows an evolution towards more Gaussian distributions for decreasing ΔT, confirming what can be seen in Fig. 7. The polar and middle regions have a highly significant positive trend ($p < .001$ in both cases). In the subtropical region, the excess kurtosis has a nonsignificant negative trend ($p = .5$).
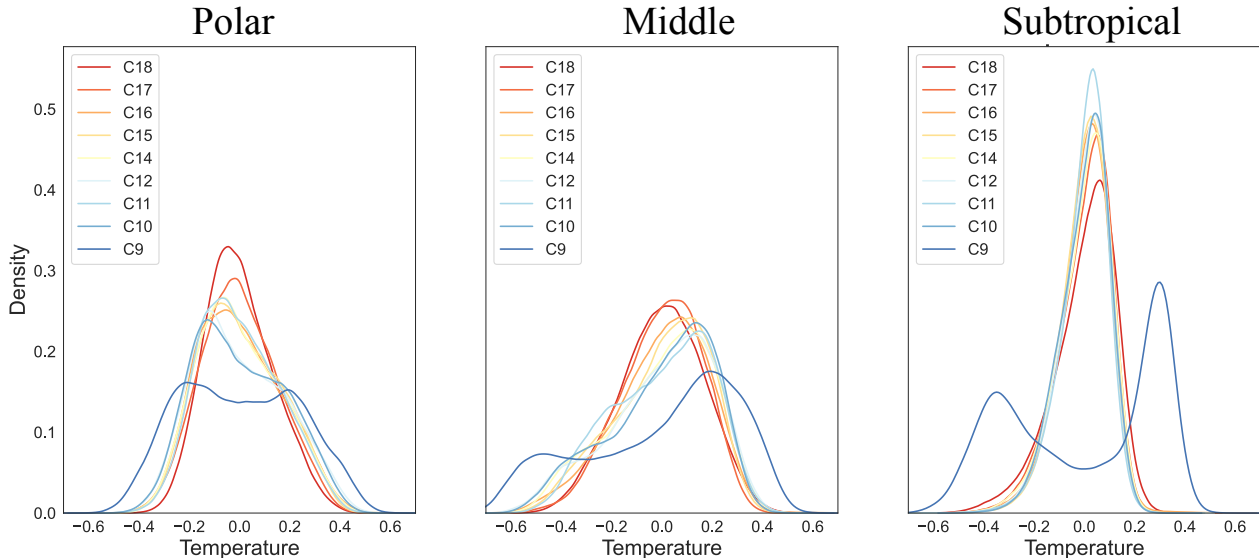
Figure 7. PDFs of temperature anomalies for the 9 experimental runs at different ΔT calculated at fixed latitudes 'p' (left), 'm' (middle), and 'e' (right), see figure 6 for the regions in the annulus.

The skewness (Fig. 8 middle) is relatively robust under changes in ΔT: the polar data possess a right (positive) and the subtropical data a left (negative) skew without any significant trend. This opposite sign for the skewness is also observed in Garfinkel and Harnik (2017) in the case of measurements of near-surface tropospheric temperatures. Moreover, the skewness behaviour reminds us of the results by Belmonte and Libchaber (1996), who found for turbulent Rayleigh-Bénard convection that the temperature distribution skewness has a positive value at the cold (top) boundary and becomes more and more negative close to the warm (bottom) boundary. Belmonte and Libchaber (1996) attribute the observation of the negative skewness to the passing of a cold thermal front originating from the thermal boundary layer.

The skewness (Fig. 8 middle) does not show a statistically significant trend for any of the regions investigated. Linz et al. (2018) studied the effects of decreasing ΔT on temperature distributions in an idealised advection-diffusion model and concluded that whilst a smaller ΔT reduces the variance, it does not have any direct effect on the skewness and kurtosis. Changes in the kurtosis should be attributed to a response to changes in the flow field instead. Therefore, the lack of a clear trend in skewness in our data agrees with the results by Linz et al. (2018).

Our experimental data clearly show a relation between the decrease in meridional temperature difference and temperature variability. These results are consistent with what was found by Dai and Deng (2021) in model simulations and reanalysis data. Their analysis indicates that Arctic amplification decreases the temperature variability over the northern mid-high latitudes.

What does the reduction in temperature variability mean in terms of extreme events? Narrower and more symmetric probability distributions imply that cold and warm extreme events become weaker with decreasing ΔT. It follows that extreme events decrease in intensity in polar and middle regions whilst near the subtropics, they become stronger. However, this does
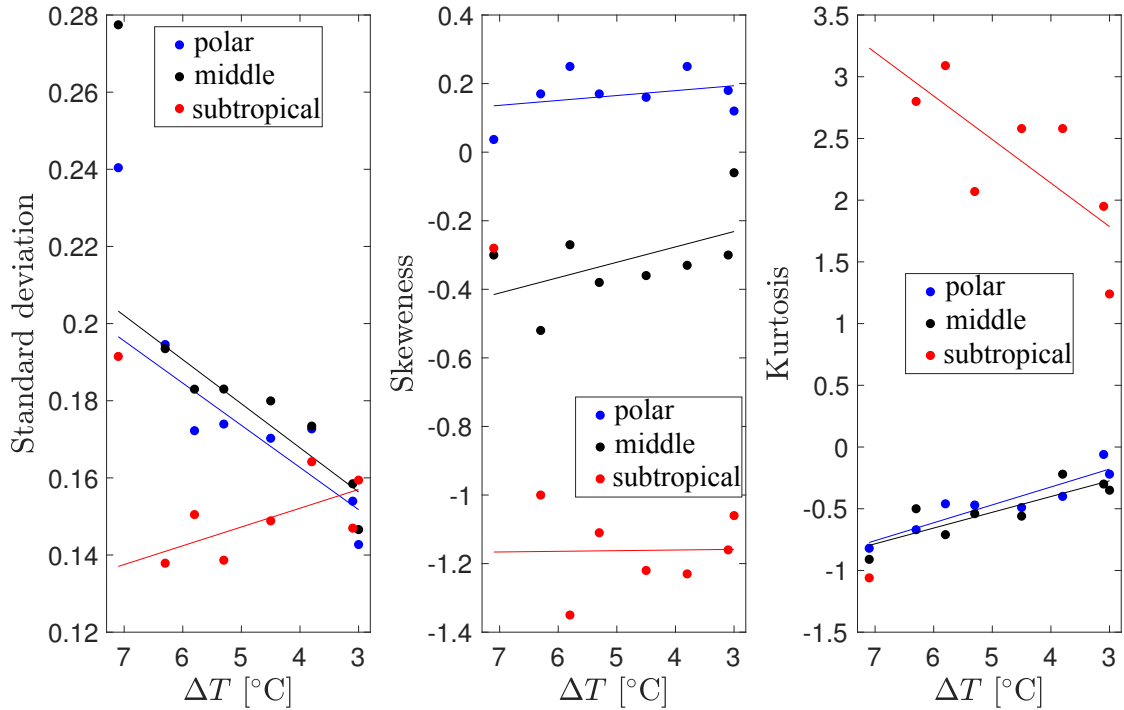
Figure 8. Standard deviation, skeweness and excess kurtosis trends for decreasing ΔT for the inner most ring (blue dots), the middle ring (black dots), and the outer ring (red dots).

not help predict extreme events' duration or frequency. In the next section, we analyse the impact of changes in ΔT on the frequency of extreme events.

4.1 Extreme event frequency

Extreme events are defined using a variety of metrics such as temperature thresholds and indices. The thresholds can be defined in different ways, the most common distinction being between relative thresholds (for example, defined by using specific percentiles of distribution or more straightforward measures like standard deviation) or absolute thresholds (for example, days with temperatures exceeding 35°) (Seneviratne et al., 2021). Therefore, the choice of the definition used to calculate extreme events can affect the meaning of extremes and possibly the results.

We have discussed in section 4 that the reduction in meridional temperature difference impacts the temperature variability and results in milder extreme temperatures from the poles to the mid-latitudes, whilst at low latitudes, the extremes might become stronger. To study whether this variability reduction impacts the frequency of extreme events, we define extreme temperature events based on a relative threshold. We chose such threshold as the standard deviation (σ) calculated for each
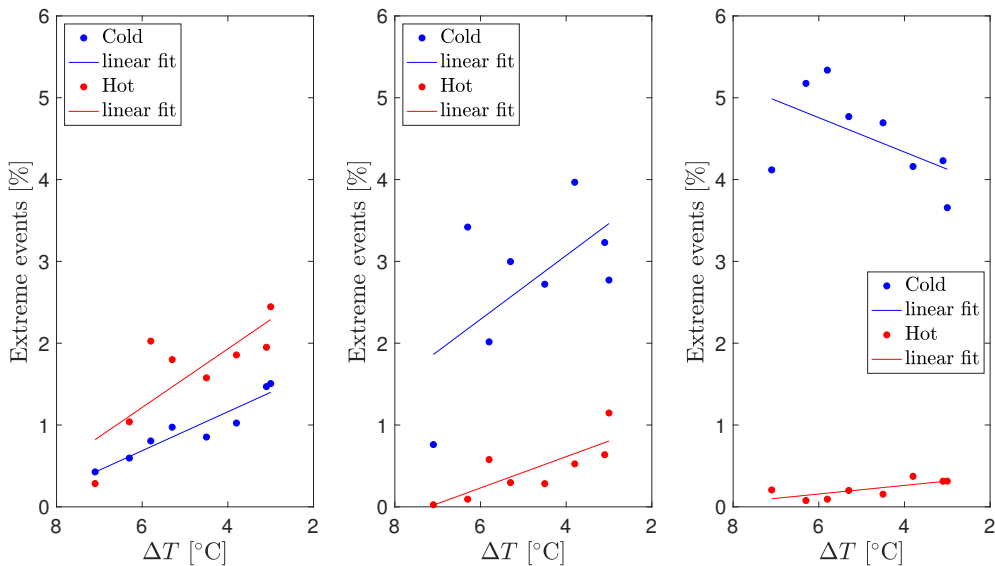
Figure 9. Trend of the cold (blue) and hot (red) extreme events with decreasing equator-pole temperature difference. The trends are considered at three latitudes in the plot: polar latitude (left), mid-latitude (middle), and subtropical latitude (right). The three latitudes are indicated in figure 10 by the labels 'p', 'm', and 'e', respectively.

experimental run, corresponding to a fixed ΔT, on ensembles of data measured at fixed latitudes. We then call extreme cold/hot events all temperatures such that $|T - T_{\text{mean}}| > 2\sigma$.

Note that the $\sigma-$threshold is latitude-dependent. The extreme event frequency is defined as the number of times the temperature crosses the set threshold normalised by the total length of the data set (which is, in any case, the same for all the data sets considered). The event duration is neglected, i.e. only the number of measurements ("days") where the temperature exceeds the threshold is counted, without distinguishing whether such days are consecutive or isolated.

The number of extreme events as a function of ΔT is plotted in Fig. 9 at the three locations 'p' (in the left plot), 'm' (in the middle plot), and 'e' (in the right plot). The cold events are plotted in blue and the hot events in red. By comparing the three plots, one can immediately notice that the number of extreme cold and hot events is similar in the region near the pole (left figure). Still, the extreme cold events become increasingly frequent, moving towards the subtropics (middle and right plots). The second noticeable feature is that the hot extreme events show a statistically significant trend for all three regions ($p = .016$ in the left plot, $p = .016$ in the right plot, $p = .036$ in the right plot in figure 9. This gives evidence for a hot extreme events increment for decreasing ΔT. For the cold extremes, the left plot reveals a statistically significant positive trend ($p < .001$), the middle plot a positive trend as well, but it is statistically nonsignificant ($p = .055$), whilst the right plot shows a statistically nonsignificant negative trend ($p = .08$).

This difference in the cold trends can be partially explained by the fact that the baroclinic wave dynamics do not govern the subtropical dynamics, and we have already suggested that the extreme event distribution along the inner regions is tightly
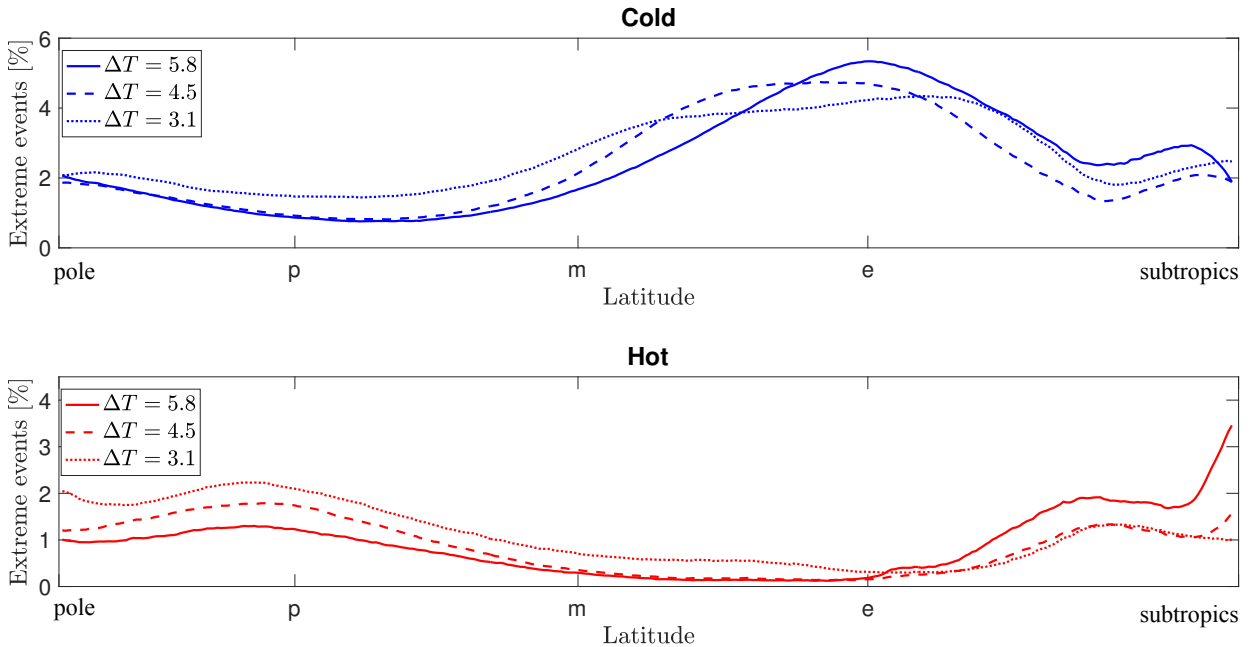
Figure 10. Number of extreme event (in percentage) as a function of latitude in the experiment. The upper plot depicts the cold events, whilst the bottom plot depicts the hot events. The lines are: solid for the experiment at $\Delta T = 5.2K$, dashed at $\Delta T = 3.8K$, dash-dot line at $\Delta T = 3K$. The labels 'p', 'm', and 'e' indicate the latitudes at which the trends shown in figure 9 are taken (see figure 6 to visualise their position).

linked to the baroclinic waves. The decrease in cold events is consistent with a possible change in the subtropical extension of the baroclinic wave.

265   For a complete understanding, we also study how extreme events are distributed as a function of latitude. For this analysis, temperatures at fixed latitudes are collected into sets, where each set is constituted by 1.2×10^6 temperature measurements for different times and longitudes. The standard deviation σ is calculated for each set, and, successively, the extreme event frequency is calculated as a function of the latitude.

     The distributions are plotted in Fig. 10 for three experiments, namely at $\Delta T = 5.2K$ (solid line) $\Delta T = 3.8K$ (dashed line)
270 and $\Delta T = 3K$ (dashed-dotted line). For easier visualisation, these three experiments have been chosen to represent the entire data set. The excluded data show similar results. The upper plot presents the extreme cold events, whilst we see the extreme hot events in the lower plot. Three latitudes labelled 'p', 'm', and 'e' are indicated on the $x-$axis for better readability.

     For both plots, we notice that the three curves have similar shapes from the polar latitudes up almost to the point 'e', with more frequent extreme events for decreasing ΔT. Yet, the cold and hot extremes exhibit opposite trends: the cold event
275 frequency increases from the pole towards the subtropics with a maximum just before 'e' and then decreases, whilst the extreme hot events behave the opposite. To some extent, the existence of a local maximum for warm and minimum for cold events at
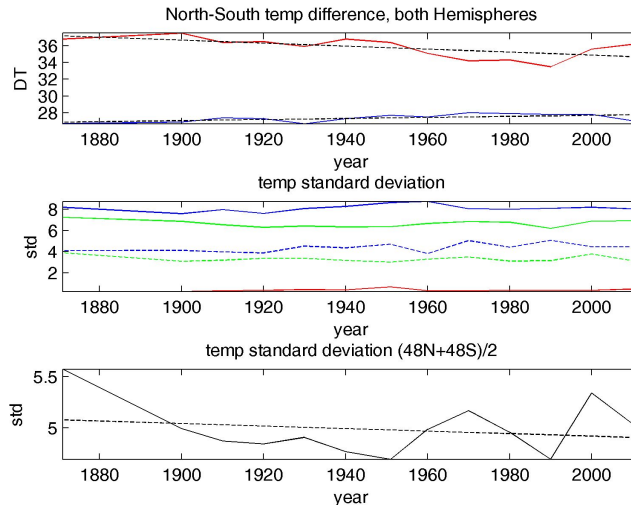
Figure 11. NCEP reanalysis data of 500hPa temperature. Upper figure: ΔT trend from 1871 to 2012, northern Hemisphere (blue), southern Hemisphere (red). The linear regression (dashed line) shows a trend towards smaller North-South temperature differences in the southern Hemisphere $(T(2012) - T(1871) = -2.51K)$ but a slightly larger difference for the northern Hemisphere $(T(2012) - T(1871) = 0.88K)$. Center figure: zonal mean temperature standard deviations for $88°N$, $88°S$ (blue solid, blue dashed), $48°N$, $48°S$ (green solid, green dashed), and equatorial (red). Bottom figure: mid-latitude zonal mean temperature standard deviation of $((T(48°N) + T(48°S))/2)$ (solid line) and linear regression (dashed line). There is a weak trend towards decreasing standard deviation $(\sigma_T(2012) - \sigma_T(1871) = -0.18K)$.

latitude 'e' can be understood by looking at figure 6, where the latitude 'e' (dotted line) marks the limit of the extension of the baroclinic wave cold tongues, covering approximately three-quarters of the gap width. The external ring (between 'e' and the 'subtropics' in the figure) is unreached by the cold tongues; therefore, we can expect differences concerning extreme event

280 frequency in this part of the annulus where we find no baroclinic wave activity. In this outer region, heat transport is mainly due to this meridional circulation, with some minor transport that might come from boundary layer instabilities and turbulent diffusion (von Larcher et al., 2018). The location of the maximum/minimum in cold/warm event frequency coincides with the utmost latitude to which the baroclinic waves extend. This clearly indicates that the baroclinic wave activity shapes the frequency distribution.

285 In summary, we suggest that the large-scale baroclinic wave dynamics govern the extreme event spatial frequency distribution in the laboratory experiment.

5 High-variability events in NCEP data

After analysing the lab data for changes in variability and the distributions of high-variability events as a function of the North-South temperature gradient, it is instructive to see what atmospheric data show concerning changes in variability and variability

290 extremes. We use the National Centers for Environmental Prediction (NCEP) reanalysis data (Kalnay and collaborators, 1996).
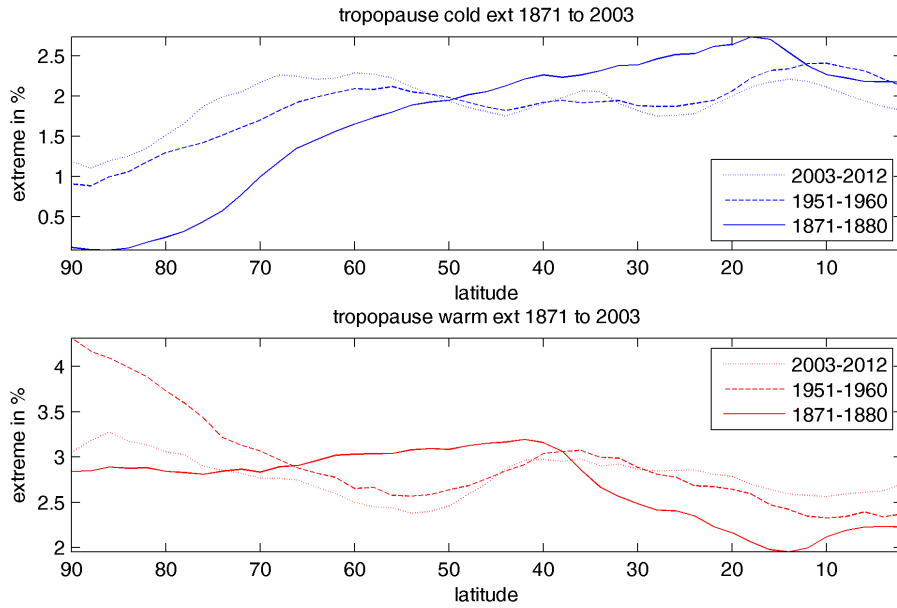
Figure 12. NCEP reanalysis data of tropopause temperature. Tropopause data have been chosen since the frequency spectra of the baroclinic wave experiment look most similar to tropopause spectra (Rodda and Harlander, 2020). A number of extreme events in % for different time slices and latitudes. The upper and bottom plots depict extreme cold and hot events, respectively. The lines are: solid for 1871-1880, dashed for 1951-1960, and dotted for 2003-2012. The seasonal cycle has been removed from the data. The extreme values have been taken from the Pacific sector (weak land-sea contrast), and the frequencies from the southern and northern Hemisphere have been averaged for any latitudinal circle.

In contrast to operational counterparts, the reanalysis data do not suffer from inhomogeneities introduced by changes in the data assimilation system. In this respect, they are a good supplement to data based on individual instrumental records or climate-model simulations (Uppala et al., 2008). Moreover, reanalysis data cover historical data as well. We use two temperature data sets from the collection "NOAA-CIRES 20th Century Reanalysis, version 2, Daily Averages", covering the period from 1871 to 2012. The first set is the daily ensemble mean pressure level data (1000hPa to 10hPa), from which we extracted just the 500hPa level. The second set is the daily ensemble mean tropopause data. We start by considering the gradient and the standard deviation of the 500hPa temperature from 1871 to 2012.

The upper panel of Fig. 11 shows the trend in the North-South temperature difference (ΔT) taken from the NCEP 500hPa data for the Northern Hemisphere (blue line) and the Southern Hemisphere (red line). These temperature gradients are evaluated from the zonal mean temperature at $88°N$ ($88°S$) and the equatorial zonal mean temperature. We see that there is no significant change for the 500hPa data in the Northern Hemisphere, except for a decline starting from the year 2000. In contrast, there is a long-term negative trend for the Southern Hemisphere. Despite some variability, the linear regressions (dashed lines) show a statistically significant trend towards more considerable North-South temperature differences for the

northern ($T(2012) - T(1871) = 0.88K$, $p = .042$) and smaller North-South temperature differences for the Southern Hemisphere ($T(2012) - T(1871) = -2.51K$, $p = .021$). It is surprising at first glance that we do not see more clearly the warming of the Arctic (Arctic amplification) in the Northern Hemispheric data. However, the warming is pronounced particularly in surface data. For the lower stratosphere, the Arctic region is even cooled due to climate change (Stendel et al., 2021) and, as shown in the upper panel of Fig. 11, according to the NCEP data, even for the 500hPa level, the warming is not obvious. This discrepancy between the change of the North-South temperature gradient for low and high levels of the troposphere drives the debate whether climate change leads to more or less wavier jet streams (Stendel et al., 2021).

The central figure displays the time evolution of the temporal standard deviation σ_T at different latitudes (blue solid, $88°N$; blue dashed $88°S$; green solid, $48°N$; green dashed, $48°S$; red, equator). The Northern Hemisphere exhibits a more significant variability, which might be related to a stronger land-sea contrast. For the mid-latitude time series, a small temporal decline can be seen (green lines), and the course of the curves looks very similar for both Hemispheres. In the bottom figure, we highlight this trend by plotting just the mid-latitude zonal mean, the standard deviation of $(T(48°N) + T(48°S))/2$ (solid line) and adding the linear regression (dashed line). Obviously, there is a weak but statistically not formally significant trend toward decreasing standard deviation ($\sigma_T(2012) - \sigma_T(1871) = -0.18K$, $p = .49$). Though not formally significant, this trend is consistent with other model data (Rind et al., 1989) and therefore it might still be physically significant. These observations are also in qualitative agreement with the results from the laboratory experiment.

To inspect the frequency of high-variability (extreme) events, we focused on NCEP reanalysis data of the tropopause temperature. These data are less prone to the effects of land-sea contrasts and might be closer to the lab experiment. Rodda and Harlander (2020) have shown that spectra from tropopause data are comparable to the frequency spectra of the baroclinic wave experiment, and we suggest a similar connection concerning extreme values. We highlighted three ten-year periods: 1871 to 1880, 1951 to 1960, and 2003 to 2012. The seasonal cycle has been removed from the data. The frequency of extreme values, defined as values larger or smaller than twice the standard deviation, has been calculated for all longitude circles with an increment of $20°$. Subsequently, for enhancing the robustness of the analysis, we took the mean of the Northern *and* Southern Hemisphere frequencies and finally we zonally averaged the frequency data. This gives the mean frequency of extreme values as a function of latitude ranging from $90° - 0°$.

We see from Fig. 12 that the number of extremes, broken down to values above (warm, red curves) or below (cold, blue curves) the 2σ standard deviation threshold, ranges between 1 and 4%. For the cold case, the frequency of extreme events is larger at low latitudes, i.e. 1.7% to 2.5% in the latitude band from $30°$ to $10°$ and 0.25% to 2% in the latitude band from $80°$ to $60°$. We can see that the period 2003-2012, with the smallest North-South temperature gradient, shows most extremes for polar latitudes (dotted blue line, $90°$ to $60°$) but least for tropical latitudes (dotted blue line, $20°$ to $0°$). Note that the experimental data lack a tropical dynamics (f-plane with a wall as a southern boundary). Hence, one must be careful when comparing low-latitude NCEP data results with experimental data close to the heated outer sidewall. For the warm extremes, we see the highest frequency for the period 1951-1960 (dashed red line) near the polar region (more than 4%). In this polar region, the most recent period shows more extreme warm events (dotted red line) than the historical data (solid red line) but about 1% less than the

period 2003-2012 (dashed red line). Obviously, for the frequency of extreme events, the strongest North-South gradient can be found for the decade 1951-1960 (dashed red line).

340   Comparing the experimental data (Fig. 10) with the NCEP data (Fig. 12) we find a notable qualitative similarity of the curves from 'p' to 'e' and from about $90°$ to $20°$, respectively. Cold/warm extreme events occur more at low/high latitudes, in agreement with what was observed by Garfinkel and Harnik (2017). Furthermore, the cold events in NCEP and experimental data with large ΔT are most numerous at low latitudes. The frequency decreases for lessening ΔT. In contrast, cold events are most probable for smaller ΔT for near-polar and equatorial latitudes. It should be noted that the NCEP data (Fig. 12)

345   do not show such distinct extreme event peaks around the near equator region but have a monotonic increase/decrease for cold/hot events instead. This difference can be expected since the appearance of a local peak in the experiment might be due to the mentioned missing tropical dynamics, as previously explained. Note further that the largest ΔT experiment gives a very regular baroclinic wave (see figure 3 a), somewhat unrealistic with respect to atmospheric flows. Caution is, therefore, required when comparing the $\Delta T = 5.2$ experiment with atmospheric temperature data.

6 Conclusions

350   We have presented a series of experiments with a differentially heated rotating annulus to model a global warming scenario. Our study aims to reproduce the Arctic warming and study the possible effects on other atmospheric phenomena. For this simple experimental environment, the impact of a reduced pole-to-equator temperature difference on the mid-latitude large-scale dynamics and consequences for the likelihood and distribution of extreme events could be isolated from various processes

355   that, in a more complex way, might play a role also for the Earth's atmosphere.

We found that the jet stream becomes more irregular due to warming the pole, making it challenging to identify a clear dominant azimuthal wavenumber. Moreover, the eastward propagating speed of the meandering baroclinic jet decreases, which, for the experiment, is a consequence of a slow down of the westerly mean flow for reduced ΔT. The decreasing meridional temperature difference also leads to a reduction of the temperature variability in regions of the experiment where the baroclinic

360   waves drive the dynamics. These regions, corresponding to polar and mid-latitudes, are characterised by temperature distributions that become narrower and more symmetric. Towards the outer ring of the annulus, corresponding to subtropical regions, the dynamics is less affected by the baroclinic, and consequently, the variability shows a slight increase. Our experimental findings agree with the recent analysis of coupled model simulations and ERA5 reanalysis by Dai and Deng (2021).

The consequence of a reduced temperature variability is that extreme events tend to become milder. However, our experiment

365   also reveals that extreme cold/warm events tend to become more frequent. Furthermore, these events are larger in number at lower/higher latitudes independently of the time period and temperature differences considered in agreement with NCEP data and with measurements of near-surface tropospheric temperature reanalysis data (Garfinkel and Harnik, 2017).

We think the results of the study underpin the usefulness of the laboratory approach to understanding specific processes of climate change, in particular with a view to temperature variability and extreme events. However, we have only taken a

370   first step and more sophisticated aspects like the use of extreme value theory, long-term memory effects, heavy tails in the

amplitude of fluctuations, power-laws, spatial correlations and teleconnections etc., have been neglected in the work presented here. Moreover, a more recent and bigger rotating tank has proven to be closer to the atmospheric case than the smaller system used here (Rodda et al., 2020). Hence, further experiments using this bigger differentially heated rotating tank and a deeper statistical analysis are planned for the future to add more experimental data to observations and climate simulations.

Appendix A: Heating and cooling in the experiment

375

In this appendix, we give more details about how the heating and cooling devices of the experiment work and how the thermal equilibrium of the experiment is reached.

The water is circulated in the inner cylinder by pipes connecting it to an external device where the water is cooled to a set temperature and then pumped back. The temperature is, therefore, regulated by the thermostat. The outer ring hosts heating

380 wires that heat the water. For all experimental runs, we kept the power supplied to the wires in the outer cylinder fixed and changed the temperature in the cooling thermostat. The system is then allowed to reach the thermal equilibrium before rotation is started. Figure A1 shows the time series of the temperature measured with sensors placed in the inner (in blue) and outer (in red) rings. It can be noticed that when rotation is started (grey vertical line), the temperatures in both baths have reached an equilibrium and remain stable for the entire duration of the experiment. From these considerations, we can conclude that the

385 boundary conditions at the two conductive walls are of constant temperatures. Increasing the temperature in the inner cylinder increases the equilibrium temperature of the working fluid in the middle gap and, consequently, the equilibrium temperature for the hot bath (as it can be seen in Fig. A1).

(a)   (b)
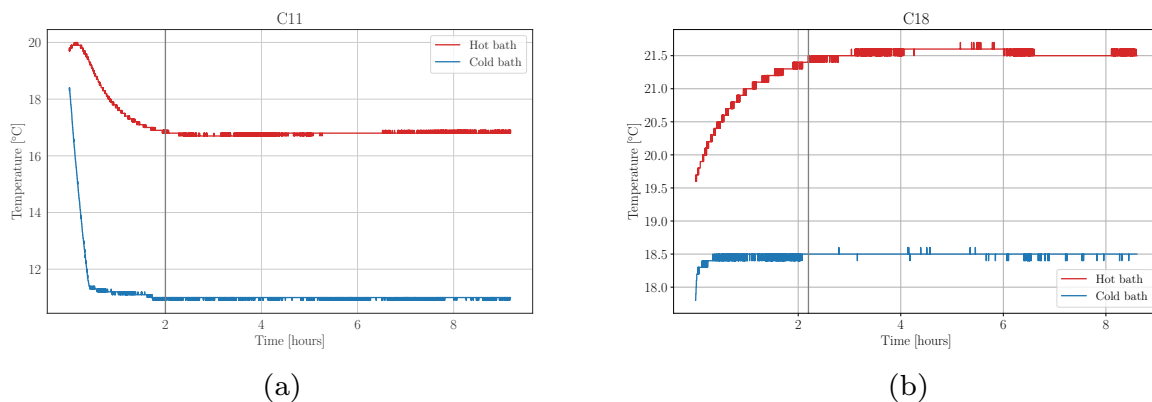
Figure A1. Time series of the temperatures measured in the outer (red) and inner (blue) rings for the experiments C11 (a) and C18 (b). The vertical grey line marks when the tank is set into rotation.

Data availability. The NCEP reanalysis data are from https://psl.noaa.gov/data/gridded/data.20thC_ReanV2c.pressure.html. We used two temperature data sets from the collection "NOAA-CIRES 20th Century Reanalysis, version2, Daily Averages", covering the period from 1871 to 2012. The first set is the daily ensemble mean pressure for the 500hPa level. The second one is the daily ensemble mean tropopause data set.

Author contributions. All authors have contributed to conceiving and designing the experiments. C.R. has run the experiments and analysed the experimental data. U.H. has analysed the NCEP data. C.R. and U.H. have drafted the paper. All authors have reviewed the manuscript and given final approval for publication.

Competing interests. The authors declare that they have no competing interests.

Acknowledgements. This work was supported by the *Spontaneous Imbalance Project* (HA 2932/8-1 and HA 2932/8-2), which is part of the research group *Multiscale Dynamics of Gravity Waves* funded by DFG (FOR1898). The work of M.V. was supported by the National Research, Development and Innovation Office (NKFIH) of Hungary under grant FK125024.

References

400 Belmonte, A. and Libchaber, A.: Thermal signature of plumes in turbulent convection: the skewness of the derivative, Phys. Rev. E, 53, 4893–4898, 1996.

Benzi, R., Salzmann, B., and Wiin-Nielsen, A. C.: Anomalous Atmospheric Flows and Blocking, Academic Press, 1986.

Blackport, R. and Screen, J. A.: Insignificant effect of Arctic amplification on the amplitude of midlatitude atmospheric waves, Science, 6, eaay2880, 2020.

405 Dai, A. and Deng, J.: Arctic amplification weakens the variability of daily temperatures over northern middle-high latitudes, Journal of Climate, 34, 2591–2609, 2021.

Dai, A. and Song, M.: Little influence of Arctic amplification on mid-latitude climate, Nature Climate Change, 10, 231–237, 2020.

Eady, E. T.: Long waves and cyclone waves, Tellus, 1, 33–52, 1949.

Fein, J. S.: An experimental study of the effects of the upper boundary condition on the thermal convection in a rotating, differentially heated

410 cylindrical annulus of water, Geophysical & Astrophysical Fluid Dynamics, 5, 213–248, 1973.

Francis, J. A. and Vavrus, S. J.: Evidence for a wavier jet stream in response to rapid Arctic warming, Environmental Research Letters, 10, 014 005, 2015.

Früh, W.-G. and Read, P.: Wave interactions and the transition to chaos of baroclinic waves in a thermally driven rotating annulus, Philosophical Transactions of the Royal Society of London A: Mathematical, Physical and Engineering Sciences, 355, 101–153, 1997.

415 Garfinkel, C. I. and Harnik, N.: The Non-Gaussianity and Spatial Asymmetry of Temperature Extremes Relative to the Storm Track: The Role of Horizontal Advection, Journal of Climate, 30, 445 – 464, 2017.

Harlander, U., v. Larcher, T., Wang, Y., and Egbers., C.: PIV- and LDV-measurements of baroclinic wave interactions in a thermally driven rotating annulus, Exp. Fluids, 51, 37–49, 2011a.

Harlander, U., von Larcher, T., Wang, Y., and Egbers, C.: PIV-and LDV-measurements of baroclinic wave interactions in a thermally driven

420 rotating annulus, Experiments in fluids, 51, 37–49, 2011b.

Hassanzadeh, P., Kuang, Z., and Farrell, B. F.: Responses of midlatitude blocks and wave amplitude to changes in the meridional temperature gradient in an idealized dry GCM, Geophysical Research Letters, 41, 5223–5232, 2014.

Hide, R.: An experimental study of thermal convection in a rotating liquid, Philosophical Transactions of the Royal Society of London A: Mathematical, Physical and Engineering Sciences, 250, 441–478, 1958.

425 Hide, R. and Mason, P. J.: Sloping convection in a rotating fluid, Advances in Physics, 24, 47–100, 1975.

Kalnay, E. and collaborators: The NCEP/NCAR 40 year reanalysis project, Bulletin of the American Meteorological Society, 77, 437–471, 1996.

Linz, M., Chen, G., and Hu, Z.: Large-scale atmospheric control on non-Gaussian tails of midlatitude temperature distributions, Geophysical Research Letters, 45, 9141–9149, 2018.

430 Overland, J. E., Dethloff, K., Francis, J. A., Hall, R. J., Hanna, E., Kim, S.-J., Screen, J. A., Shepherd, T. G., and Vihma, T.: Nonlinear response of mid-latitude weather to the changing Arctic, Nature Climate Change, 6, 992–999, 2016.

Petoukhov, V., Rahmstorf, S., Petri, S., and Schellnhuber, H. J.: Quasiresonant amplification of planetary waves and recent Northern Hemisphere weather extremes, Proceedings of the National Academy of Sciences, 110, 5336–5341, 2013.

Read, P., Pérez, E., Moroz, I., and Young, R.: General Circulation of Planetary Atmospheres: Insights from Rotating Annulus and Related
Experiments, in: Modeling Atmospheric and Oceanic Flows: Insights from Laboratory Experiments and Numerical Simulations, edited
by von Larcher, T. and Williams, P. D., chap. 1, pp. 9–44, Wiley, 2014.

Rind, D., Goldberg, R., and Ruedy, R.: Change in climate variability in the 21st century, Climatic Change, 14, 5–37, 1989.

Rodda, C. and Harlander, U.: Transition from Geostrophic Flows to Inertia–Gravity Waves in the Spectrum of a Differentially Heated
Rotating Annulus Experiment, Journal of the Atmospheric Sciences, 77, 2793–2806, 2020.

Rodda, C., Hien, S., Achatz, U., and Harlander, U.: A new atmospheric-like differentially heated rotating annulus configuration to study
gravity wave emission from jets and fronts, Experiments in Fluids, 61, 2020.

Screen, J. A. and Simmonds, I.: Amplified mid-latitude planetary waves favour particular regional weather extremes, Nature Climate Change,
4, 704–709, 2014.

Seneviratne, S. I., Zhang, X., Adnan, M., Badi, W., Dereczynski, C., Di Luca, A., Ghosh, S., Iskandar, I., Kossin, J., Lewis, S., et al.: Weather
and climate extreme events in a changing climate, Climate Change, pp. 11–1, 2021.

Stendel, M., Francis, J., White, R., Williams, P. D., and Woollings, T.: Chapter 15 - The jet stream and climate change, in: Climate Change
(Third Edition), edited by Letcher, T. M., pp. 327–357, Elsevier, third edition edn., https://doi.org/https://doi.org/10.1016/B978-0-12-
821575-3.00015-3, 2021.

Stuecker, M. F., Bitz, C. M., Armour, K. C., Proistosescu, C., Kang, S. M., Xie, S.-P., Kim, D., McGregor, S., Zhang, W., Zhao, S., et al.:
Polar amplification dominated by local forcing and feedbacks, Nature Climate Change, 8, 1076–1081, 2018.

Uppala, S., Simmons, A., Dee, D., Kållberg, P., and Thépaut, J.-N.: Climate Variability and Extremes during the Past 100 Years, chap.
Atmospheric Reanalyses and Climate Variations, Springer, 2008.

Vincze, M. and Jánosi, I. M.: Laboratory experiments on large-scale geophysical flows, in: The Fluid Dynamics of Climate, pp. 61–94,
Springer, 2016.

Vincze, M., Borchert, S., Achatz, U., von Larcher, T., Baumann, M., Liersch, C., Remmler, S., Beck, T., Alexandrov, K. D., Egbers, C.,
Froehlich, J., Heuveline, V., Hickel, S., and Harlander, U.: Benchmarking in a rotating annulus: a comparative experimental and numerical
study of baroclinic wave dynamics, Meteorologische Zeitschrift, pp. 611–635, 2015.

Vincze, M., Borcia, I. D., and Harlander, U.: Temperature fluctuations in a changing climate: an ensemble basedexp erimental approach, Sci.
Reports, 254, DOI:10.1038/s41 598–017–00 319–0, 2017.

von Larcher, T. and Egbers, C.: Experiments on transitions of baroclinic waves in a differentially heated rotating annulus, Nonlinear Processes
in Geophysics, 12, 1033–1041, 2005.

von Larcher, T., Viazzo, S., Harlander, U., Vincze, M., and Randriamampianina, A.: Instabilities and small-scale waves within the Stewartson
layers of a thermally driven rotating annulus, Journal of Fluid Mechanics, 841, 380–407, 2018.

Wallace, J. M., Deser, C., Smoliak, B. V., and Phillips, A. S.: Climate Change: Multidecadal and Beyond, chap. Attribution of climate change
in the presence of internal variability, World Scientific, 2014.